J. Fluid Mech. (2015), *vol.* 768, *pp.* 442–467.
doi:10.1017/jfm.2015.99

Dynamics of sessile drops. Part 2. Experiment

Chun-Ti Chang[1,†], J. B. Bostwick[2], Susan Daniel[1,3] and P. H. Steen[1,3,4]

[1]Theoretical and Applied Mechanics, Cornell University, Ithaca, NY 14853, USA

[2]Department of Engineering Science and Applied Mathematics Northwestern University, Evanston, IL 60208, USA

[3]School of Chemical and Biomolecular Engineering, Cornell University, Ithaca, NY 14853, USA

[4]Center for Applied Mathematics, Cornell University, Ithaca, NY 14853, USA

(Received 27 July 2014; revised 5 February 2015; accepted 8 February 2015)

High-speed images of driven sessile water drops recorded under frequency scans are analysed for resonance peaks, resonance bands and hysteresis of characteristic modes. Visual mode recognition using back-lit surface distortion enables modes to be associated with frequencies, aided by the identifications in Part 1 (Bostwick & Steen, *J. Fluid Mech.*, vol. 760, 2014, pp. 5–38). Part 1 is a linear stability analysis that predicts how inviscid drop spectra depend on base state geometry. Theoretically, the base states are spherical caps characterized by their 'flatness' or fraction of the full sphere. Experimentally, quiescent shapes are controlled by pinning the drop at a circular contact line on the flat substrate and varying the drop volume. The response frequencies of the resonating drop are compared with Part 1 predictions. Agreement with theory is generally good but does deteriorate for flatter drops and higher modes. The measured frequency bands agree better with an extended model, introduced here, that accounts for forcing and weak viscous effects using viscous potential flow. As the flatness varies, regions are predicted where modal frequencies cross and where the spectra crowd. Frequency crossings and spectral crowding favour interaction of modes. Modal interactions of two kinds are documented, called 'mixing' and 'competing'. Mixed modes are two pure modes superposed with little evidence of hysteresis. In contrast, modal competition involves hysteresis whereby one or the other mode disappears depending on the scan direction. Perhaps surprisingly, a linear inviscid irrotational theory provides a useful framework for understanding observations of forced sessile drop oscillations.

Key words: drops, drops and bubbles

1. Introduction

Manipulation of drops facilitates numerous applications, including inkjet printing (Castrejon-Pita *et al.* 2013), atomization (Qi *et al.* 2010), enhanced heat conduction (Daniel, Chaudhury & Chen 2001), particle patterning (Wright & Saylor 2003; Whitehill *et al.* 2010) and mixing within droplets (Shilton *et al.* 2008). Manipulation may occur by means of acoustic fields (Marston & Apfel 1980), electric fields

† Email addresses for correspondence: phs7@cornell.edu, cc836@cornell.edu

(Trinh, Holt & Thiessen 1996), magnetic fields (Hill & Eaves 2012) or by means of mechanically induced pressure fields (e.g. by piezoelectric constriction, Basaran 2002) or accelerations (e.g. by shaking, Rodot, Bisch & Lasek 1979). In regimes where inertia and surface tension compete, drop manipulation often involves drop oscillations. An understanding of drop resonance is important for developing applications, either to maximize droplet motions by forcing or to avoid undesired oscillations.

This paper primarily reports experimental tests of the theoretical predictions of Bostwick & Steen (2014) (Part 1). In Part 1, the resonant behaviour of a drop sitting on a solid substrate was solved for. The context is a linear stability analysis of spherical-cap base states parameterized by contact angle (CA) α. In the analysis, the contact line (CL) may be pinned, mobile or some combination thereof. The case relevant to the experiments reported below is a pinned CL, in which case α serves as a proxy for the drop volume. Henceforth, all theory results refer to the pinned CL case unless otherwise noted. For a given α, the mode shapes and natural frequencies are predicted by the stability analysis and the countably infinite set of frequencies constitutes the spectrum for that α. The α family of spectra can be related to breaking the symmetry of the classical Rayleigh–Lamb (RL) spectrum for free drops (Lamb 1932; Rayleigh 1879). Varying α splits the classical RL spectrum and shifts the frequencies upward or downward.

Mode shapes also vary with α and hence are deformed from the RL version of the mode shapes. The RL terminology $[k, l]$, originating from a spherical harmonics description, can be carried over to the deformed shapes: 'zonal' for axisymmetric modes (longitudinal wavenumbers $l = 0$), 'sectoral' for star-shaped modes ($k = l$) and 'tesseral' for all other modes ($k \geqslant l > 0$). This is because analogous wavenumbers arise from the separation of variables that applies for the solution of the underlying Laplace equation for shapes periodic in the longitudinal direction (l). In short, our problem reduces to a Sturm–Liouville-like boundary-value problem in the co-latitudinal direction with solution having characteristic k and depending on l through the separation constant ((3.1), Part 1). It should be noted that the restriction $k + l =$ even arises to ensure no penetration at the base of the spherical cap (cf. Part 1).

Steady symmetry breaking of a spherical drop can be induced by means other than introducing a solid support. Busse (1984) considers drop rotation and reports that frequency splitting generated by centrifugal and Coriolis effects can shift frequencies of zonal modes either upward or downward, depending on whether the steady distortion is to an oblate or prolate spheroid respectively. Feng & Beard (1991) consider a charged drop exposed to an external electric field and report a downward shift for zonal modes and an upward shift for sectoral modes. Shi & Apfel (1995) consider an acoustically levitated drop and report how the accompanying steady deformation shifts the frequency of oscillations initiated by a sound pulse.

Experimental studies to compare with these theoretical/computational predictions are rare because Earthbound experiments require drop levitation that typically couples to the frequency response. Levitation is easier in low gravity but experimental opportunities there are limited (Shen, Xie & Wei 2010). Sessile drop vibrations offer an easily controlled symmetry breaking from the RL spectrum that is uncoupled from the shaker-table forcing and thus provides a relatively simple Earthbound context to study frequency shifts.

The literature on drop oscillations is vast. We offer a brief overview only. The first observation of RL modes is reported for Leidenfrost drops by Holter & Glasscock (1952). The RL frequency predictions are tested experimentally for immiscible drops

by Trinh, Zwern & Wang (1982), drops in microgravity by Wang, Anilkumar & Lee (1996) and levitated drops by Trinh *et al.* (1996), Perez *et al.* (1999) and Shen *et al.* (2010). Rodot *et al.* (1979) reports similar mode shapes for sessile drops. Rayleigh's prediction for the oscillating free drop still sees widespread use even in situations where the drop is not completely free, as for a drop levitated (Hill & Eaves 2010; Brunet & Snoeijer 2011) or in contact with a solid (Daniel, Chaudhury & de Gennes 2005; Dong, Chaudhury & Chaudhury 2006; Noblin, Kofman & Celestini 2009; Chebel, Risso & Masbernat 2011) or with another liquid (Dorbolo *et al.* 2008). Modifications, *ad hoc* or otherwise, to RL theory are often invoked to account for the influence of the substrate on the drop frequency (Yoshiyasu, Matsuda & Takaki 1996; Perez *et al.* 1999; Sharp, Farmer & Kelly 2011). Our previous experiments (Chang *et al.* 2013) document the limitations of the RL frequencies for non-RL situations, especially for the higher modes of sessile drops.

The experiments reported in Chang *et al.* (2013) have limited experimental control over the tested shapes: for those experiments, $\alpha \sim 70°$. This paper has a broader scope. We introduce a surface preparation technique that pins the CL to a circular footprint. This enables us to experimentally vary the shape by varying the volume: here, $35° \leqslant \alpha \leqslant 135°$. The actual placed volume of the drop can be measured by its α from a side view of the static drop. Or, because of the good pinning, a volume measurement can replace the α measurement using the explicit trigonometrical relationship, (1.2), Part 1. The CA is also chosen in Part 1 as the preferred parameterization. For consistency with Part 1, we continue to use α as the preferred parameterization. It should be kept in mind that dynamical shapes have dynamical contact angles that differ from α.

A first result of this paper is the comparison of measured to predicted frequency shifts with α, over the range of CAs. A second result introduces forcing and viscosity using a viscous potential flow (VPF) extension to the theoretical model in order to account for discrepancies between experiment and theory, observed for higher modes and flatter drops. As a third result, we report on modal interactions which arise because of overlap between resonant frequency bands. Whether frequencies are related harmonically or subharmonically and whether their resonance bands overlap is important to the nature of the interaction. Two kinds of interactions are documented: one that appears to be a linear superposition which we call 'mode mixing' and another that exhibits hysteresis where one mode dominates which we call 'mode competition'. As an extension of the single α probed in our previous paper (Chang *et al.* 2013), the first topic is new. The second results are completely new. The third topic is made possible by the range of α probed and, hence, is also new, even though mixing is mentioned in Chang *et al.* (2013).

In Part 1, disturbances to the base state are assumed to be normal modes $y\mathrm{e}^{\mathrm{i}\omega t}$. This assumption leads to a linear eigenvalue problem for the reduced disturbance shape y,

$$-\omega^2 M[y] + K[y] = 0, \tag{1.1}$$

where M is a positive definite operator representing the drop's inertia (mass) and K is an operator representing its capillarity (spring constant). These correspond to (3.2) in Part 1. Part 1 solves (1.1) for eigenvalues $\omega_{k,l}$ and corresponding eigenmodes $y_{k,l}$. Schematically, $\omega_{k,l}^2 = \langle y_{k,l}, K[y_{k,l}]\rangle / \langle y_{k,l}, M[y_{k,l}]\rangle > 0$ if the operator K is positive definite. The corresponding motion is oscillatory with frequency $\omega_{k,l} = \pm\sqrt{\langle y_{k,l}, K[y_{k,l}]\rangle / \langle y_{k,l}, M[y_{k,l}]\rangle}$, which is the case for drops with pinned CLs.

Pinning of drops is achieved by chemical means and/or by substrate roughening. Drops are driven by plane-normal substrate motion at frequencies f and amplitudes A experiencing acceleration a, where $a \equiv (2\pi f)^2 A$ (cf. figure 1). Droplet response

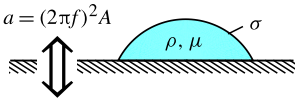

FIGURE 1. (Colour online) A sessile drop with density ρ, dynamic viscosity μ and surface tension σ is subject to substrate oscillation of frequency f, amplitude A and acceleration $a = (2\pi f)^2 A$.

(*a*) Physical parameters

Frequency (f)	Amplitude (A)	Acceleration (a)
30–1100 Hz	1–430 μm	0.1–100g

(*b*) Dimensionless parameters

Frequency	Ohnesorge	Reynolds, forcing	Bond, forcing
$\lambda \equiv 2\pi f(\rho r^3/\sigma)^{1/2}$	$\epsilon \equiv \mu/\sqrt{\rho r \sigma}$	$Re \equiv ar/fv$	$Bo_a \equiv \rho a r^2/\sigma$
2.5–100	0.0024	75–2000	0.075–80

TABLE 1. Parameters of response and forcing by plane-normal displacement $A\sin(2\pi ft)$ where the amplitude $A = a/(2\pi f)^2$. The inverse Ohnesorge number, ϵ^{-1}, is a response Reynolds number. For water, $\rho = 1000$ kg m^{-3}, $\sigma = 72$ mN m^{-1}, $\mu = 10^{-3}$ Pa s and $\nu \equiv \mu/\rho$.

is observed by high-speed imaging. Resonance peaks are detected using frequency scans at fixed a using various protocols. Frequencies are extracted by image analysis and depend on visual mode recognition. For non-axisymmetric modes (non-zonals), mode identification must be by top view. Identification is crucial for frequency band measurement. For this reason, we include § 4.2 on mode discovery and identification, which complements § 6 of Part 1, and which reproduces some material of Chang *et al.* (2013), for completeness.

Water is used as the droplet liquid because of its relatively high surface tension σ and low dynamic viscosity μ. Drop size is chosen small enough that undisturbed shapes are nearly spherical but large enough for reasonable image resolution. That is, $r \leqslant (\sigma/\rho g)^{1/2}$, where r is the pinned footprint radius and ρg is the droplet weight per volume. This leads to our water droplets having 5 mm ($\alpha < 105°$) and 2.5 mm ($\alpha > 105°$) footprint diameters. The image resolution of our optical set-up is approximately 10 μm pixel^{-1}. Scale bars throughout are set by the 50 μm linewidth of the physical grid pattern. Lengths are scaled with the footprint radius r and times with the capillary time scale $(\rho r^3/\sigma)^{1/2}$. It should be noted that for all the results reported here, both the driving and the response Reynolds numbers are $\gg 1$, consistent with a dominant inviscid behaviour (table 1).

Even for water, however, viscous effects are not negligible as estimated by the Ohnesorge number $\epsilon \equiv \mu/(\rho r \sigma)^{1/2}$. Viscosity is incorporated into the theory of Part 1 using the VPF approximation (Joseph 2003, 2006; Padrino, Funada & Joseph 2007). This leads to a modified operator equation,

$$-\gamma^2 M[y] + \mathrm{i}\gamma\epsilon C[y] + K[y] = 0, \tag{1.2}$$

where ω of (1.1) has been replaced by $\gamma \equiv \omega + \mathrm{i}\beta$ and C is a dissipation operator. Under- and over-damped oscillations familiar from mass–spring–damper dynamical

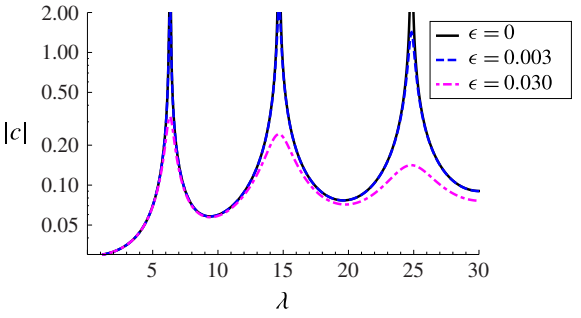

FIGURE 2. (Colour online) Influence of forcing and viscosity on the resonance peaks. As for a single-degree-of-freedom mechanical oscillator (see, for example, p. 51 of Hartog (1956)), the resonance peaks are lowered by damping. This particular plot represents a result of the theory of § 5 below. The amplitude $|c|$ is plotted against the forcing frequency λ for the zonal [2, 0], [4, 0] and [6, 0] modes, left to right, as it depends upon the Ohnesorge number ϵ, with $\alpha = 70°$. For the experiments reported in this paper, $\epsilon \leqslant 0.003$.

systems may be anticipated. A similar approach has been adopted in Bouwhuis *et al.* (2013) to illustrate the resonance of levitated drops.

Forcing by the moving substrate requires an additional extension. When the moving boundary is explicitly included in the formulation (Bauer 1992), assumptions about the drop's response must be made to proceed with the analysis. We follow the approach for Faraday oscillations (Benjamin & Ursell 1954) and model the forcing as occurring through the drop's bulk pressure, as $F_0 e^{i\lambda t}$. This reduces the time-dependent problem to the forced–damped extension of the reduced harmonic oscillator operator (1.1),

$$-\lambda^2 M[y] + i\lambda\epsilon C[y] + K[y] = F_0. \tag{1.3}$$

Another way of thinking about this approximation is that we purposefully circumvent modelling the interaction between the drop and the forcing agent, which could be a plate vibrating plane-normal or plane-tangent, an ultrasonic pulse, an air pulse or even a voltage trigger. By ignoring the nature of the forcing agent, we lose any information about the phase lag or subharmonic/supraharmonic nature of the response relative to the driving signal. However, what is lost in fidelity to experiment may be gained in generality of results. For the experiments reported here, zonal modes ($l = 0$) oscillate at the forcing frequency and hence are harmonics, whereas non-zonals ($l \neq 0$) oscillate at half the forcing frequency and thus are subharmonics, as discussed in Chang *et al.* (2013). Predictions of the forced VPF theory (1.3) are illustrated in figure 2, where drop response is plotted as a function of frequency for the first three zonal modes, $[k, l] = [2, 0]$, $[4, 0]$ and $[6, 0]$. The three resonant peaks exhibit infinite amplitude for $\epsilon = 0$, but are dramatically lowered even for viscosity as weak as $\epsilon = 0.03$.

Figure 2 is a paradigm for how forcing broadens spectral lines to resonance bands and how viscosity lowers the otherwise infinite resonance peak. This is like what occurs for the discrete mass–spring–damper system of elementary mechanics. In addition to being paradigmatic, figure 2 represents a result from the VPF theory below and will be mentioned later in § 5.

We mention here another useful paradigm in anticipation of our later discussion of resonance band protocols (§ 3): the amplitude response for the Mathieu equation as it

depends on forcing frequency (Benjamin & Ursell 1954; Arscott, Sneddon & Ulam 2014). This plot identifies 'resonance tongues', where growth of the parametrically driven oscillator occurs. Outside such tongues, the response does not grow.

Two kinds of modal interactions are reported at the end of this paper: mixing and competing. Mode mixtures can be interpreted as the superposition of inviscid modes. On the other hand, competition is detected while probing frequency crossing of half-frequency subharmonic modes. This phenomenon is hysteretic and depends on the history of the forcing frequency. Both mixing and competing occur because of frequency band overlap and spectral crowding. Experiments and theory consistently suggest that both phenomena depend sensitively on α. Their main difference is that mixing can be understood as linear superposition of modes. In contrast, competition is hysteretic and hence nonlinear.

A similar mixing phenomenon has been suggested by Vukasinovic, Smith & Glezer (2007). They report that, when the forcing amplitude is increased, an axisymmetric mode shape first emerges and then persists to mix with a lattice mode. Numerous works report similar phenomena for Faraday waves. For example, Batson, Zoueshtiagh & Narayanan (2013) report stable co-dimension 2 points on the spectrum where two mixing modes may or may not be of the same harmonic type. In experiments with viscous liquids, Rajchenbach, Clamond & Leroux (2013) observed mixing of star-shaped patterns whose behaviours are independent of the container's shape.

In what follows, we first introduce our experimental set-up in § 2, including both the hardware set-up and the surface treatments. Frequency measurement protocols are reported in § 3. In § 4, we present the 37 modes observed to date and the technique for discovering these pure modes. Then we compare inviscid predictions with experiments regarding frequency crossing. The inviscid predictions are extended by the VPF theory developed in § 5. We compare experimentally observed frequency bands with VPF predictions in § 6. Mode mixing and mode competition are discussed in § 7. Finally, a brief conclusion is provided in § 8.

2. Experimental hardware

2.1. *Opto-mechanical imaging platform*

The mechanical oscillation platform and observation apparatus are shown in figure 3. The sessile drop motion is driven by a single-frequency sine wave (VTS-100 mechanical vibrator, by Vibration Testing Systems, Aurora, OH, USA). Mirrors are installed to visualize the motion using one high-speed camera (RedLake HG-XL, by Integrated Design Tools, Inc., Tallahassee, FL, USA). A woven metal mesh is sandwiched under the solid substrate that holds the drop. Light is projected directly from underneath the mesh. The drop surface refracts the light according to how the surface deforms and the thus-deformed mesh is viewed from the top. The optical train can also be rotated to view from the side. The optics provides spatial resolutions of 10 μm pixel^{-1} at 5000 f.p.s. and 15 μm pixel^{-1} at 10 470 f.p.s. Features down to 40 μm can be clearly resolved on the platform. Further detail may be found in Chang *et al.* (2013).

2.2. *Substrates*

Two different substrates with circular pinning (P) sites are prepared. One substrate is glass (gl), P_{gl}, and the other polycarbonate (PC), P_{PC}. The substrates P_{gl} and P_{PC} constrain drops over different ranges of α (table 2). Fixing the footprint of a drop has

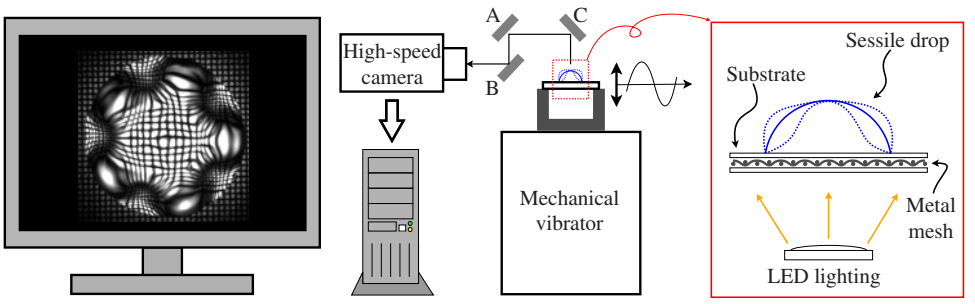

FIGURE 3. (Colour online) Schematic of the imaging platform. Shown in the red (rightmost) box are the key components: the mesh pattern and the LED light source under the drop. Light rays from the LEDs are refracted by the drop's deforming surface, reflected into the high-speed camera by mirrors A, B and C, and convey a deformed mesh pattern to the computer, thereby visualizing the deformation of the drop's surface. A signal generator (not shown) oscillates the surface sinusoidally in the direction perpendicular to the plane of the surface.

Substrate	P_{gl}	P_{PC}	H_{gl}
Base	Glass	Polycarbonate (PC)	Glass
Site radius, $2r$ (mm)	5	2.5	None
Pin site interior	Smooth bare glass	Smooth fluorinated PC	Smooth aminated glass
Pin site exterior	Smooth fluorinated glass	Rough fluorinated PC	Smooth aminated glass
Contact angle (deg.)	35–105	105–135	60–80
Drop volume (μl)	10–46	10–28	20

TABLE 2. Substrate characteristics.

the advantage of volume control, as mentioned above. We prescribe α by fixing the base radius r and controlling the volume V. For spherical caps, the volume V relates to α as $V/r^3 = (\pi/3)(2\text{–}3\cos\alpha + \cos^3\alpha)/\sin^3\alpha$. In our experiments, the volume is controllable to ± 1 μl. Additionally, fixing the footprint has the advantage of not having to track the droplets across the substrate. Circular pinning sites are created by establishing a hydrophobic surface exterior to the circular hydrophilic interior. Substrate P_{gl} starts by homogeneously fluorinating a glass slide to make the entire surface hydrophobic. Afterwards, the coating is removed within a circle of desired size by masking the exterior region and plasma treating the interior, as depicted in figure 4. Alternatively, substrate P_{PC} starts with a PC base surface, masks a circular footprint, roughens the exterior region by solvent-induced recrystallization (Cui *et al.* 2012) and homogeneously fluorinates the entire surface. More details can be found in appendix A. Most of the experiments reported here use the two pinning substrates.

A third substrate is prepared on glass without pinning sites, H_{gl}. It was used previously by Chang *et al.* (2013) and is retained for overlap with those experiments. Substrate H_{gl} is prepared by homogeneously (H) aminating a glass slide to yield $\alpha \sim 70°$ for water over the entire surface. The idea behind H_{gl} was to have a surface that gave a consistent α. It turns out that H_{gl} exhibits sufficient stick–slip that the CL acts as if it is pinned over the time scale of a shaker experiment. However, the α can vary from 60° to approximately 80°, depending on how and where the drop is

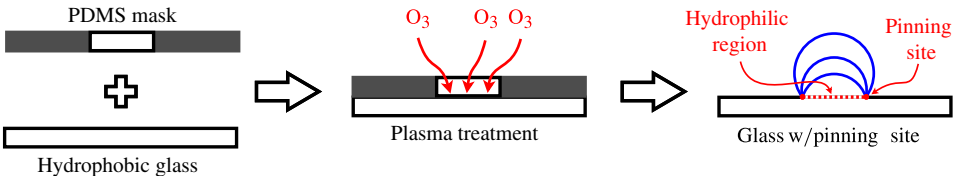

FIGURE 4. Schematic of making pinning sites on glass slides with partial plasma treatment.

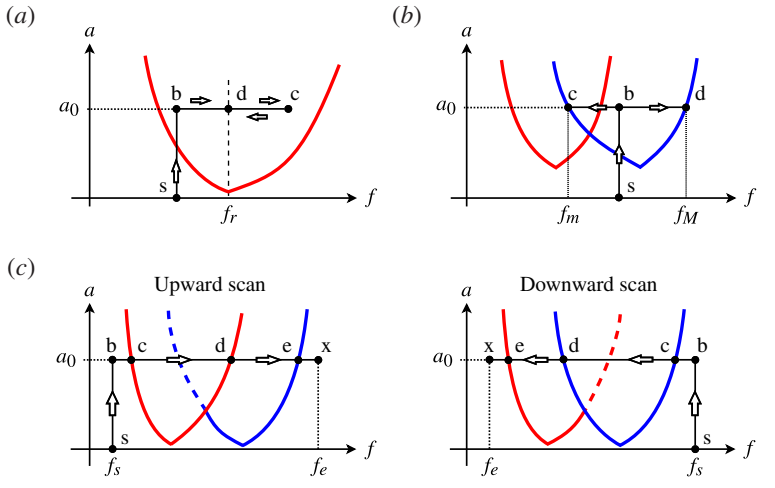

FIGURE 5. Protocols for finding (*a*) resonance, (*b*) frequency bands and (*c*) mode competition by varying the forcing frequency f and acceleration a. The curves of the same colour form a resonance tongue. All protocols start by increasing a up to a_0 while fixing f (s $\rightarrow$ b). Then a_0 is held fixed. (*a*) For zonal modes, the frequency scan (b $\rightarrow$ c $\rightarrow$ d) iteratively locates the resonance frequency f_r. (*b*) The lower and upper limits of a non-zonal mode's band are probed by a downward (s $\rightarrow$ b $\rightarrow$ c) and an upward (s $\rightarrow$ b $\rightarrow$ d) scan. (*c*) For mode competition, the automatic scan proceeds from a starting frequency (f_s) to an ending frequency (f_e), points b $\rightarrow$ x. Frequencies and mode shapes at points c, d and e are recorded. The dashed curve segments represent the mode's hidden band limit due to hysteretic competition of modes.

deposited. Therefore, the static α of each drop on H_{gl} has to be measured at the start and end of each forcing experiment. The good pinning ability of the P substrates eliminates this complication.

3. Measurement protocols

Three different protocols are adopted to measure frequencies. The first protocol is used for resonance frequencies of zonal modes, the second for frequency bands of non-zonal modes and the third for hysteretic mode competition. As sketched in the resonance tongue diagram, figure 5, all three protocols start by fixing the frequency f and ramping up the forcing to a target acceleration $a = a_0$. This corresponds to leg s $\rightarrow$ b in all plots of figure 5. Then a frequency scan at fixed a_0 follows. The choice of a_0 and other details of the frequency scan depend on how modes can be triggered and

how their deflections can be observed. These details will be described below where the protocols are used. In subsequent sections, dimensionless frequencies ω normalize the forcing frequency f with the capillary time scale

$$\omega = f\sqrt{\frac{\rho r^3}{\sigma}}2\pi h, \tag{3.1}$$

where $h = 1$ for zonal modes and $h = 1/2$ for non-zonal modes, since they are harmonic and half-frequency subharmonic modes respectively (Chang *et al.* 2013).

3.1. *Resonance frequencies of zonal modes*

The deflection of a zonal mode is directly measurable from the side view because of the axisymmetry. This allows identification of the resonance frequency f_r at which the deflection is maximized. Besides, zonal modes can be triggered at relatively small accelerations compared with the non-zonals. Therefore, in experiments, f_r is sought by the iterative frequency scan b $\rightarrow$ c $\rightarrow$ d in figure 5(*a*). Experiments with zonal modes are conducted on P_{gl}.

3.2. *Frequency bands of non-zonal modes*

Unlike zonal modes, non-zonal deflections cannot be measured by a side view. Top-view snapshots clearly visualize the mode shapes, but it remains difficult to measure the deflection in real time and identify the resonance frequency by a maximum deflection. Besides, non-zonal modes require greater forcing acceleration to trigger, and they hysteretically compete with one another when their bands overlap ('tongues' in figure 5*b*). In experiments, the forcing is first ramped up to and held fixed at an acceleration a_0 sufficient to trigger and sustain a target mode. Instead of probing f_r, two separate frequency scans b $\rightarrow$ c and b $\rightarrow$ d respectively seek the minimum f_m and maximum f_M frequencies between which the target mode persists. The range $[f_m, f_M]$ is regarded as the band of the target mode. Experiments with non-zonal modes use P_{gl} and P_{PC}.

3.3. *Hysteretic mode competition*

As will be discussed in § 7.2, non-zonal modes compete due to band overlapping and spectral crowding. The phenomenon is probed by upward and downward frequency scans, as illustrated in figure 5(*c*). A sufficient forcing acceleration a_0, a starting frequency f_s and an ending frequency f_e are prescribed first. At $f = f_s$ and $a = a_0$, the scan is triggered and proceeds at 1 Hz s^{-1} (b $\rightarrow$ x). The forcing frequency is monitored with an oscilloscope. The top view of the oscillating drop is monitored by visually inspecting the real-time video stream. Upon observing any pattern variation (at c, d and e), the shape change and the corresponding frequency measured by the oscilloscope are documented. Due to hysteresis, an excited mode tends to persist. In fact, pattern selection is observed to depend exclusively upon which mode is generated first, which in turn depends on the direction (i.e. upward or downward) of the frequency scan. In experiments on mode competition, all frequency scans are monotonic and results from upward ($f_s < f_e$) and downward ($f_s > f_e$) scans are reported separately. The protocol is designed to capture the hysteretic nature of mode competition. These experiments utilize P_{gl}.

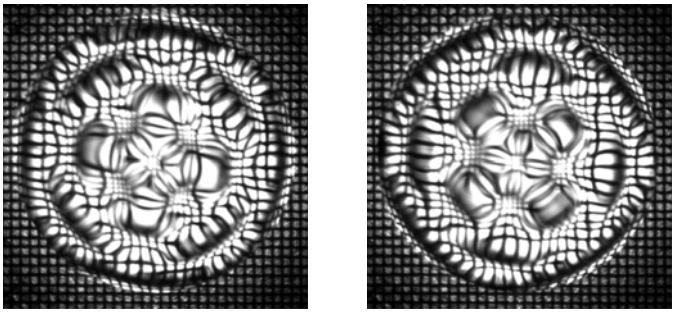

FIGURE 6. Top-view snapshots of the [10, 4] mode, which was missing from the catalogue in Chang *et al.* (2013). The two images differ by half a cycle of oscillation. The drop (16 μl) is confined by a 5 mm diameter pinning site on P_{gl}.

4. Comparison with inviscid theory

4.1. *Overview of comparison*

Here, we compare the observed mode shapes, resonance frequencies and frequency crossings with predictions. The inviscid theory of Part 1 predicts the shapes and frequencies of eigenmodes. The frequencies are predicted to vary sensitively with α. For zonal modes, flatter drops show greater spectral-line separation (figure 6*a* in Part 1). Frequency crossing and spectral crowding occur at approximately $\alpha \sim 90°$ for modes $[k, l]$ with the same k (figures 10 and 11 in Part 1). Although the inviscid theory can account for contact-line mobility, the comparisons below are restricted to pinned drops on P_{gl} and P_{PC}.

4.2. *Mode discovery and identification*

Laboratory discovery of a target mode is favoured by avoiding spectral crowding. The first substrate we used was H_{gl}, which has $\alpha \sim 70°$ for water. This was fortuitous since $\alpha \sim 70°$ reasonably separates spectral lines for most target modes (Chang *et al.* 2013).

Target modes are not always easy to discover. Namely, the $[k, l] = [10, 4]$ mode is missing in the photo gallery of the first 36 modes in Chang *et al.* (2013, figure 5). The [10, 2] and [10, 6] modes had been observed but the [10, 4] mode was elusive, despite considerable efforts to find it. The difficulty in finding the [10, 4] mode was probably due to the overlap of its band with those of other modes for $\alpha \sim 70°$. Competition between resonance modes of free surface waves is not uncommon (Ciliberto & Gollub 1985). Substrate H_{gl} was the only choice at the time. Since then, substrate P_{gl} has become available and discovery of the [10, 4] mode readily followed. The pinning sites of P_{gl} (and P_{PC}) provide more effective control over the drop's α. This precision mitigates spectral crowding. The [10, 4] mode is exhibited in figure 6, where the two images differ by half a cycle of oscillation.

The same protocol generates the other pure target modes in figure 5(*b*) of Part 1. We start with a preliminary frequency–acceleration sweep to locate a mode's band. The sweep proceeds as a random walk in the frequency–acceleration parameter space until a target mode is observed. If the mode mixes with another mode, a drop with a different α, say greater, is tested using the same procedure. In the worst case when both trials produce mixing modes, a third trial is attempted with a drop of a smaller α. A pure mode is typically isolated from mixed modes within three trials, provided that the target mode has appeared in a prior trial as part of a mixture.

Mode identification is aided by 'reading' the layers and sectors from the image, as introduced in Chang *et al.* (2013) (also § 6, Part 1). By lighting from below, hills and troughs in the deformed drop spread and focus the mesh grid respectively. The hills are particularly easy to read. For example, the [10, 4] mode in figure 6 shows four sets of four hills. The hills of each set are 90° rotationally symmetric. Each set is arranged in a concentric ring with a 45° rotational shift from the adjacent ring. The four sets give $n = 4$ layers, and four hills in each set give $l = 4$ sectors. Therefore, the [10, 4] mode has $(n, l) = (4, 4)$. Here, we adopt the convention of parentheses for the layer–sector and square brackets for spherical–harmonic classification. Layers and sectors are most recognizable in side and top views respectively, as illustrated for four examples in the lower right triangular region in figure 7. Zonal modes consist of $n \geqslant 2$ axisymmetric layers. Axisymmetry means $l = 0$ sectors. For example, the illustrated (4, 0) mode has four layers and no longitudinal variation. Sectoral modes have $n = 1$ layer with l sectors. The (1, 6) mode exhibits $n = 1$ layer with $l = 6$ sectors. Tesseral modes possess some ($l > 0$) longitudinal variation in multiple ($n > 1$) layers. The (3, 2) mode possesses $n = 3$ layers from the side view and $l = 2$ sectors from the top view. Likewise, $n = 2$ and $l = 4$ can be deduced from the side and top views of the (2, 4) mode. It should be noted that the (1, 0) photo is the top view of a static drop, for reference.

In figure 8, we compare selected modes from figure 7 with predictions. The correspondence between observed and predicted shapes is evident: the (4, 0) both exhibit two rings of troughs, the (1, 5) both exhibit a five-vertex star, the (2, 4) both exhibit a cross in a square and the (3, 5) both exhibit a five-vertex star confined by two pentagons. A more exacting comparison shows subtle differences between observed and predicted shapes for the (1, 5), (1, 6), (3, 5) and (3, 6) modes. Namely, the observed unequal magnification around the drop's centre for these modes suggests some mixing with certain zonal modes. Mode mixing is discussed in § 7.1.

The layer–sector (n, l) and spherical–harmonic $[k, l]$ (MacRobert 1967) classifications are useful for different purposes. The one-to-one correspondence is given by the relationship $(n, l) = ((k - l)/2 + 1, l)$. The (n, l) classification helps one to intuitively identify mode shapes because n gives the plane-normal and l the longitudinal wavenumber. Hence, in figure 7, the up-to-date catalogue of the first 37 modes is organized by the (n, l) classification. In contrast, the $[k, l]$ classification naturally arises in the theory and therefore is used in our subsequent frequency comparison and discussion of frequency crossings.

4.3. *Frequency comparison against inviscid theory*

For zonal modes, resonance frequencies are obtained using the protocol outlined in § 3.1. Experimental results (symbols) are plotted with inviscid predictions (lines) in figure 9(*a*). The predictions are reproduced from figure 6(*a*) of Part 1. The agreement is reasonable for $60° \leqslant \alpha \leqslant 100°$, but inviscid theory overpredicts the frequency for flatter ($\alpha < 60°$) drops. Moreover, the overprediction worsens for higher modes.

For non-zonal modes, the average $(f_m + f_M)/2$ of the lower and upper band limits $[f_m, f_M]$ is reported as the resonance frequency, measured using the protocol outlined in § 3.2. Experimental results (symbols) are plotted with inviscid predictions (lines) in figure 9(*b–d*). The inviscid predictions are reproduced from figure 11(*d,f*) of Part 1 for $k = 5, 7$ respectively, and by similar calculations for the $k = 9$ non-zonals. Much like the zonal comparison, the agreement is reasonable for $70° \leqslant \alpha \leqslant 100°$. For flatter drops and higher wavenumbers, inviscid theory again overpredicts frequencies. In order to test whether the viscosity accounts for the overprediction, we extend the theory using VPF in § 5.

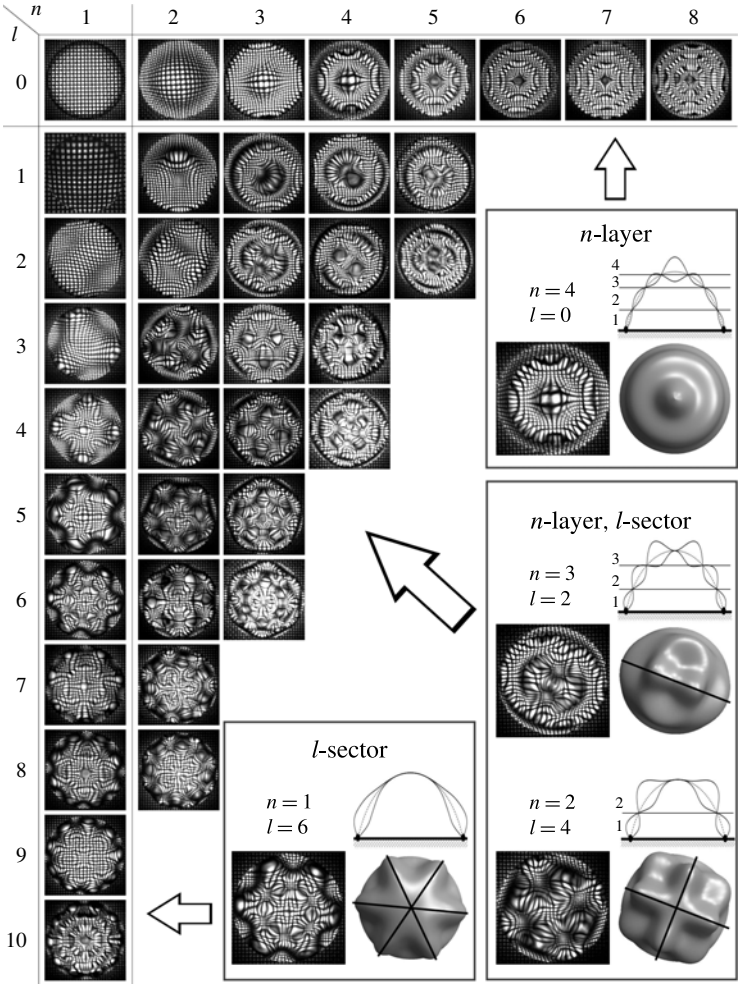

FIGURE 7. Layer–sector (n, l) identification schematic (triangular region, at right) and catalogue of top-view snapshots of the 37 modes discovered to date (triangular region, at left). For reference, $(n, l) = (1, 0)$ is the top view of a static drop. Modes $l = 0$ are zonal, $n = 1$ are sectoral, while all others are tesseral. This updates the catalogue of Chang *et al.* (2013) (figure 5) and should be compared with the predicted shapes in figure 5(*b*) of Part 1. Drops are on H_{gl} or P_{gl} with $60° < \alpha < 80°$.

4.4. *Frequency crossings against inviscid theory*

The inviscid theory predicts a frequency order that switches between sub- and superhemispherical drops. The switching occurs slightly below $\alpha = 90°$ and depends on k (figure 11, Part 1). According to the measurements shown in figure 9(*b–d*), when $\alpha < 110°$, the modes order from low to high frequencies as $[5, 5] \rightarrow [5, 3]$, $[7, 7] \rightarrow [7, 5]$ and $[9, 9] \rightarrow [9, 7] \rightarrow [9, 5]$, whereas for $\alpha > 110°$, the order reverses: $[5, 3] \rightarrow [5, 5]$, $[7, 5] \rightarrow [7, 7]$ and $[9, 5] \rightarrow [9, 7] \rightarrow [9, 9]$. Careful inspection of figure 9 suggests that crossings are predicted around $\alpha = 90°$ but are not observed

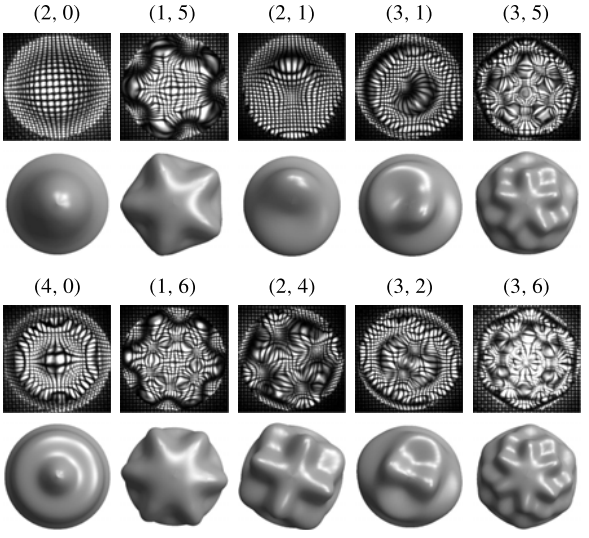

FIGURE 8. Comparison of observed (snapshots) and predicted (rendered) shapes for selected modes. Identification (n, l) by layers n and sectors l is immediate. Predictions are based on pinned CL and $\alpha = 75°$.

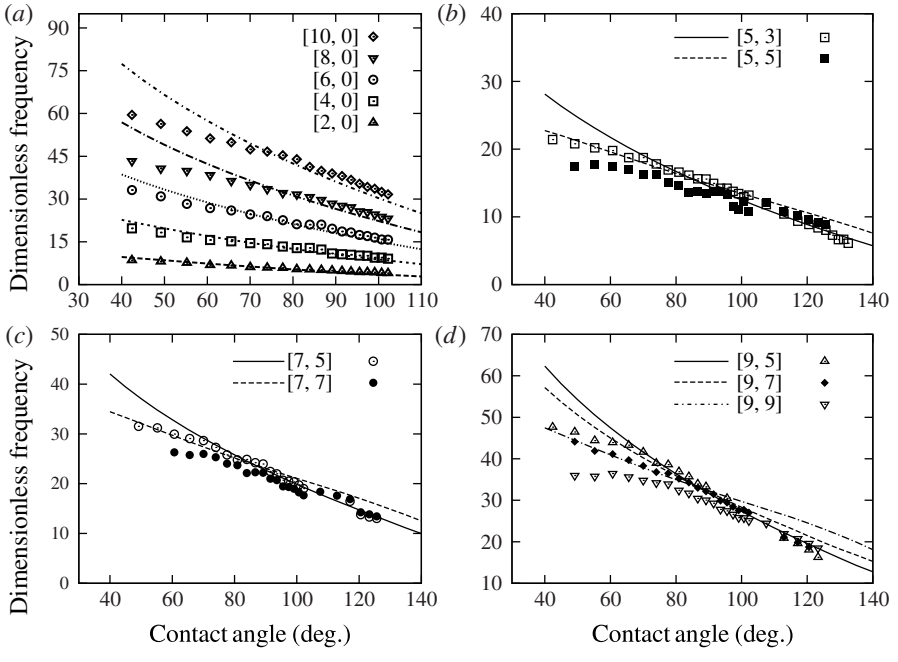

FIGURE 9. Frequency comparisons. Inviscid theory (lines) and observation (symbols) for (*a*) zonal modes, (*b*) $k = 5$ non-zonals, (*c*) $k = 7$ non-zonals and (*d*) $k = 9$ non-zonals. Note the predicted re-ordering of non-zonal modes across $\alpha \approx 90°$.

until $\alpha \approx 105°$. This may be because modes compete at approximately $\alpha \approx 90°$–$100°$ where there is spectral crowding. Since sectoral modes typically dominate other modes, the predicted mode crossing may occur but be masked due to the scavenging by sectoral or tesseral modes.

5. Theory of forced oscillations

The idea of the VPF approximation (Joseph 2003) is to insert the irrotational solution into a dissipation functional to obtain a viscous correction. The oldest such scheme goes back to Lamb (1932). We adopt a recent variation that starts by assuming that the velocity field $\boldsymbol{v} = -\nabla\Psi$ can be expressed using the velocity potential Ψ and proceeds to evaluate the dissipation from the irrotational field (?), noting that the velocity field cannot satisfy the no-slip condition on the solid support. The particular dissipation functional we evaluate is derived elsewhere (Bostwick & Steen 2013, (1.9)). For brevity, we record here the equations for a forced sessile drop.

The setting is an incompressible viscous fluid subjected to a time-dependent pressure field $p(t) = F_0 \mathrm{e}^{\mathrm{i}\Omega t}$, occupying a domain D bounded by a spherical-cap interface $\partial D^f \equiv \Gamma$ held by a constant surface tension σ and supported below by a surface ∂D^s ((2.2)–(2.4), Part 1). We assume normal modes for the interface disturbance η and velocity potential Ψ,

$$\eta(s, \varphi, t) = y(s)\mathrm{e}^{\mathrm{i}l\varphi}\mathrm{e}^{\mathrm{i}\Omega t}, \quad \Psi(\boldsymbol{x}, t) = \phi(\rho, \theta)\mathrm{e}^{\mathrm{i}l\varphi}\mathrm{e}^{\mathrm{i}\Omega t}, \tag{5.1a,b}$$

with s the arclength of the spherical cap in the co-latitudinal direction, $y(s)$ the disturbance on Γ in the radial direction, l the longitudinal wavenumber and $\Omega = 2\pi f$ the forcing frequency (in rad s^{-1}). The normal stress balance at the interface can be written as

$$\begin{aligned}\sin^2(\alpha)\left(\left(\frac{\partial\phi}{\partial n}\right)'' + \cot(s)\left(\frac{\partial\phi}{\partial n}\right)' + \left(2 - \frac{l^2}{\sin^2(s)}\right)\left(\frac{\partial\phi}{\partial n}\right)\right)\\ = \lambda^2\phi - \mathrm{i}\lambda\epsilon\boldsymbol{n}\cdot(\nabla\otimes\nabla\phi)\cdot\boldsymbol{n} + \lambda F_0,\end{aligned} \tag{5.2}$$

where $\otimes$ is the tensor product, ϵ is the Ohnesorge number and λ is the scaled forcing frequency defined in table 1. The velocity potential additionally satisfies the following auxiliary conditions ((2.13), Part 1):

$$\nabla^2\phi = 0 \ [D], \quad \frac{\partial\phi}{\partial n} = 0 \ [\partial D^s], \quad \frac{\partial\phi}{\partial n} = -\mathrm{i}\lambda y \ [\partial D^f], \quad \int_\Gamma \frac{\partial\phi}{\partial n}\mathrm{d}\Gamma = 0. \tag{5.3a–d}$$

We use the Green's function ((4.2), Part 1)

$$G(x, y; l, \lambda, \Lambda) = \begin{cases} \xi(l)y_1(y; l)\left[\dfrac{y_2(b; l)}{y_1(b; l)}y_1(x; l) - y_2(x; l)\right], & b < x < y < 1, \\ \xi(l)y_1(x; l)\left[\dfrac{y_2(b; l)}{y_1(b; l)}y_1(y; l) - y_2(y; l)\right], & b < y < x < 1, \end{cases} \tag{5.4}$$

where

$$\left.\begin{aligned} &y_1(x;0)=P_1(x), \quad y_2(x;0)=Q_1(x), \quad y_1(x;1)=P_1^{(1)}(x), \quad y_2(x;1)=Q_1^{(1)}(x),\\ &y_1(x;l\geqslant 2)=(x+l)\left(\frac{1-x}{1+x}\right)^{l/2}, \quad y_2(x;l\geqslant 2)=\frac{(x+l)}{2l\left(l^2-1\right)}\left(\frac{1+x}{1-x}\right)^{l/2}, \end{aligned}\right\} \tag{5.5}$$

with $x=\cos(s)$, $b=\cos(\alpha)$ and

$$\xi(l)\equiv\begin{cases}1/2, & l=1,\\ 1, & l\neq 1,\end{cases} \tag{5.6}$$

to write the solution to (5.2) as

$$\begin{aligned}\left(1-b^2\right)\frac{\partial\phi}{\partial n}(x) \;=\; &-\mathrm{i}\lambda\epsilon\int_b^1 G(x,y)(\boldsymbol{n}\cdot(\boldsymbol{\nabla}\otimes\boldsymbol{\nabla}\phi)\cdot\boldsymbol{n})\mathrm{d}y\\ &+\lambda^2\int_b^1 G(x,y)\phi(y)\mathrm{d}y+F_0\lambda\int_b^1 G(x,y)\mathrm{d}y,\end{aligned} \tag{5.7}$$

which is recognized as an integral equation for the velocity potential ϕ.

A solution series of the orthogonal basis functions ϕ_j,

$$\phi=\sum_{j=1}^{N}a_j\phi_j, \tag{5.8}$$

is applied to (5.7) and inner products are taken to generate a set of algebraic equations

$$\sum_{j=1}^{N}\left(m_{ij}+\mathrm{i}\epsilon\lambda\tau_{ij}-\lambda^2\kappa_{ij}\right)a_j=F_0\lambda\gamma_i, \tag{5.9}$$

with

$$\left.\begin{aligned} &m_{ij}\equiv\left(1-b^2\right)\int_b^1\left(\frac{\partial\phi_i}{\partial n}\right)\phi_j\mathrm{d}x, \quad \tau_{ij}\equiv\int_b^1\int_b^1 G(x,t)\,(\boldsymbol{n}\cdot(\boldsymbol{\nabla}\otimes\boldsymbol{\nabla}\phi_i)\cdot\boldsymbol{n})\,\phi_j(x)\mathrm{d}x\mathrm{d}t,\\ &\kappa_{ij}\equiv\int_b^1\int_b^1 G(x,t)\phi_i(t)\phi_j(x)\mathrm{d}x\mathrm{d}t, \quad \gamma_i\equiv\int_b^1\int_b^1 G(x,t)\phi_i(x)\mathrm{d}x\mathrm{d}t. \end{aligned}\right\} \tag{5.10}$$

The auxiliary conditions (5.3) are satisfied through proper selection of the basis functions ϕ_j, as discussed in §4.2, Part 1. For zonal modes,

$$\phi_j(\rho,\theta)=\rho^{2j}P_{2j}(\cos\theta)\,, \tag{5.11}$$

while for non-zonal modes,

$$\phi_j^{(l)}(\rho,\theta)=\rho^j P_j^{(l)}(\cos\theta)\,. \tag{5.12}$$

It should be noted that the damped–driven oscillator structure (5.9) can be put into the form of (1.3) using $\partial\phi/\partial n=-\mathrm{i}\lambda y$. For a fixed $\lambda,\epsilon,\alpha,l$, we compute the response a_j, ϕ_j, $\partial\phi_j/\partial n$ of the fluid. Here, we note that the response is linear in the amplitude of the applied pressure F_0. Henceforth, we report the response as $c_j\equiv a_j/F_0$. A typical response for the zonal modes is shown in figure 2. Traversing the graph from left to right, the first peak corresponds to the [2, 0] mode, while the second and third peaks are the [4, 0] and [6, 0] modes respectively.

6. Frequency comparison against VPF theory

We now compare the observed resonance bands with VPF predictions. The damped–driven correction to the inviscid theory, (1.3), predicts a response curve for the modes of each longitudinal wavenumber l. Figure 2 presents the prediction for the three lowest zonal modes. These resonance bands are interpreted as follows. For any mode, its resonance peak gives the resonance frequency. The peak is surrounded by two valleys and these frequencies define the lower and upper resonance band limits. For the lowest mode of a given l (i.e. [2, 2] for $l=2$), for which there is no neighbouring peak, the lower limit of its band is defined as the frequency at 2 % peak amplitude. In figure 10, predicted bands are plotted as greyscale and compared with the same observations in figure 9. It should be noted that the seven non-zonal frequencies are given their own plots in figure 9(*b–h*). The curve in each greyscale band is the inviscid resonant peak prediction. The protocols in §§ 3.1 and 3.2 are used to measure the frequencies of zonal and non-zonal modes respectively. A glance at figure 10 suggests that the VPF band, in contrast to the inviscid curve, adequately captures the lower frequencies for flatter drops and higher wavenumbers. We now further discuss non-zonal results, focusing on the range of α reported for each mode.

The frequencies for the $k=5$ and $k=7$ modes are presented in figure 10(*b–h*). In these experiments, the sectoral modes [5, 5] and [7, 7] disappear for flat drops with $\alpha < 50°$. Any attempt to generate the modes by increasing the forcing acceleration ends up ejecting satellite droplets without disturbing the drop's circular footprint. It should be noted that hills of sectoral modes reside along the CL. Therefore, the disappearance of the [5, 5] and [7, 7] modes is suspected to result from the enhanced influence of a pinned CL on the deflection of the free surface of flatter drops. For $90° \leqslant \alpha \leqslant 100°$, multiple modes mix and/or compete, amongst which sectoral modes typically dominate. This explains the significantly reduced bandwidths of the tesseral modes [5, 1], [5, 3], [7, 1], [7, 3] and [7, 5] over this range. Further increasing α separates the spectra of these modes. For superhemispherical drops, the patterns of [5, 3], [5, 5], [7, 5] and [7, 7] remain recognizable. In contrast, identification of the [5, 1] and [7, 1] modes becomes difficult, because from the top view only the topmost peak is clearly observable yet that peak resembles that of a zonal mode. Features below a drop's equator cannot be identified from the top view, hence the absence of the [5, 1] and [7, 1] modes for $\alpha > 110°$. For [7, 3], it is suspected that the mode either requires a much higher acceleration to excite, or it simply gets scavenged by other modes. For all experiments seeking the $k=7$ modes of drops on P_{PC}, no clear triangular pattern is ever observed at any α. From the frequencies in figure 10, VPF theory adequately predicts the bands for the $k=5$ and $k=7$ modes. In particular, it should be noticed that a reasonable agreement is achieved even for $\alpha < 60°$. Similar results for the $k=9$ non-zonal modes are presented in appendix B.

A certain subjectivity in the protocol must be acknowledged. The frequency at which each mode appears and disappears depends on the driving acceleration a. Increasing acceleration is observed to broaden bands (cf. figure 5). For each mode, we choose the smallest acceleration consistent with unambiguous recognition of the appearance/disappearance of that mode shape. Lower modes typically require lower a_0. For the seven non-zonals just discussed, a range of 20–25g is suitable. That is, the bands predicted by the VPF theory adequately approximate the observed resonance of drops excited by $a_0 = 20$–$25g$. For the higher modes discussed in § 7.2, the range of a_0 must be widened to $a_0 = 20$–$35g$.

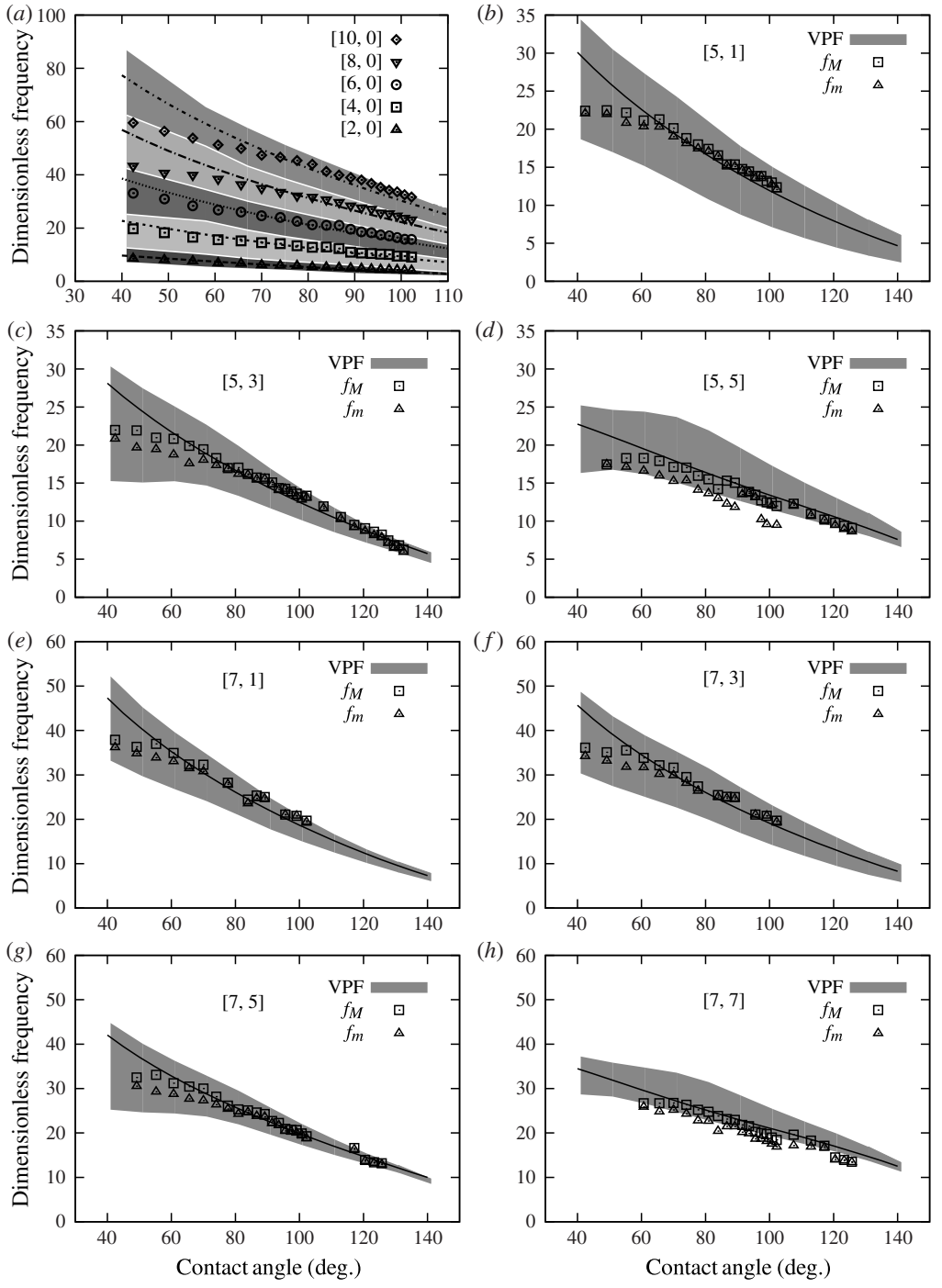

FIGURE 10. Frequency comparisons: VPF theory (shaded bands), inviscid theory (solid lines) and observation (symbols) for (*a*) zonal modes and (*b–h*) non-zonal modes $[k, l]$ for $k = 5,\ 7$ and $l \leqslant k$ $(k + l =$ even). For each mode, f_M and f_m are the observed upper and lower limits of the band.

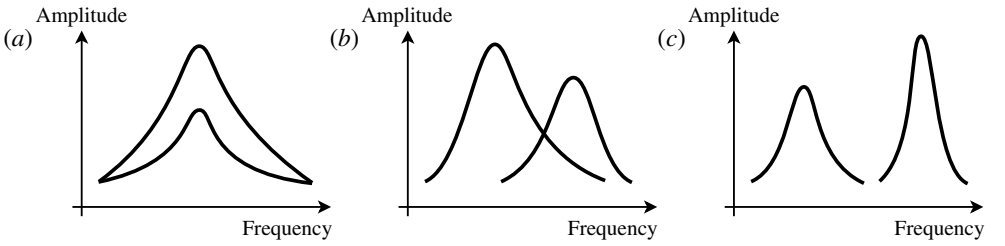

FIGURE 11. Schematics of band interactions: response amplitude against forcing frequency illustrating (*a*) complete overlap, (*b*) partial overlap and (*c*) no overlap of bands.

7. Mode interactions

In experiments, forcing causes finite bandwidths of response, and the extent of band overlap correlates with modal interactions. Figure 10 clearly shows the finite bands. As schematically illustrated in figure 11, the bands of any two modes can (*a*) completely overlap, (*b*) partially overlap or (*c*) completely disjoin. In cases (*a–b*), modes can either compete when $\alpha \sim 90^\circ$ or mix as mentioned in § 6. The signature of competition is hysteresis, whereas the signature of mixing is coexistence by superposition. To illustrate mode mixing, we provide four examples. In each, an observed mixture can be decomposed into two pure modes. To illustrate mode competition, we document the evolution of band overlap between modes that hysteretically compete when their bands cross one another.

7.1. *Mode mixing*

Mode mixing is frequently observed. Here, we describe the mixing of a harmonic zonal mode with a half-frequency subharmonic non-zonal mode. Such mixtures are typical observations (>90%), although mixtures of two non-zonal modes have been seen.

Examples of mixed and pure mode shapes are presented in figure 12. For the zonal mode of each mixing pair, the superscript '$-$' or '$+$' indicates concavity or convexity of the drop's centre in the image respectively. This is a reference for the phase of the oscillation. For the $(5, 0)$ mode to be added to mixture A, for example, the magnified mesh at the drop's centre suggests local convexity, and hence $(5, 0)^+$. Because mixture A shows a concave centre, adding $(5, 0)^+$ to the mixture recovers the pure shape of the $(2, 3)$ mode. Similarly, as mixture D exhibits a convex centre, recovery of a pure $(2, 7)$ mode from mixture D requires the addition of $(8, 0)^-$ to the mixture.

7.2. *Mode competition*

Clear signs of nonlinearity are revealed in experiments with subhemispherical drops. Frequency crossings near $\alpha = 90^\circ$ are discussed in § 4.3. Crossings at lower CAs are also predicted by the inviscid theory. For drops with $60^\circ \leqslant \alpha \leqslant 80^\circ$, modes with $k = \{5, 6, 7\}$ and $\{7, 8, 9\}$ are predicted to cross. However, only crossings for $k = \{7, 8, 9\}$ have been observed. The reason for the undetected $\{5, 6, 7\}$ is not known. The observed frequency crossings also reveal hysteretic mode competitions, as now discussed.

Crossings of modes (i) [7, 3] and [8, 8] and (ii) [8, 2], [8, 4] and [9, 9] are investigated. These two sets are predicted and repeatedly observed, probably because

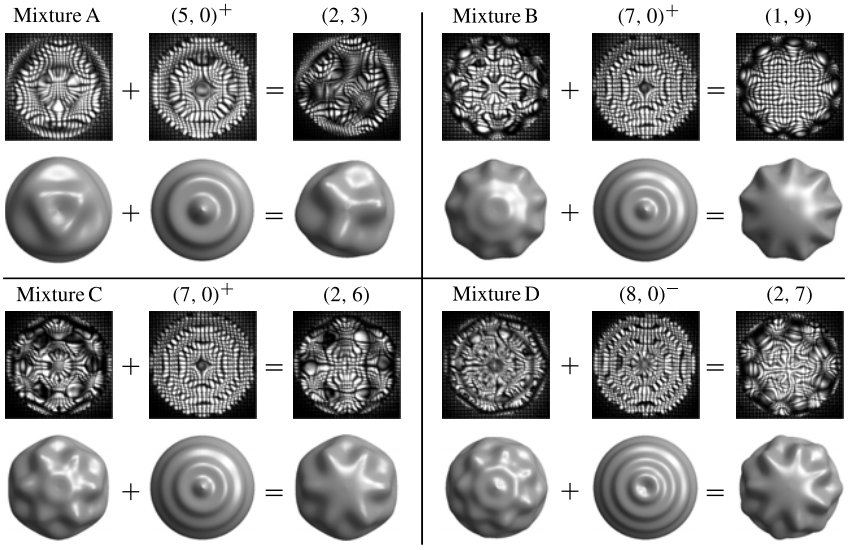

FIGURE 12. Mixed and pure modes: snapshots (top row) and rendered shapes (bottom row) for four examples A–D (panels). Mixtures A–D are superposed with a pure mode of appropriate phase shift to yield a different pure mode. The superscript '−' or '+' indicates concavity or convexity respectively of the drop's centre in the image.

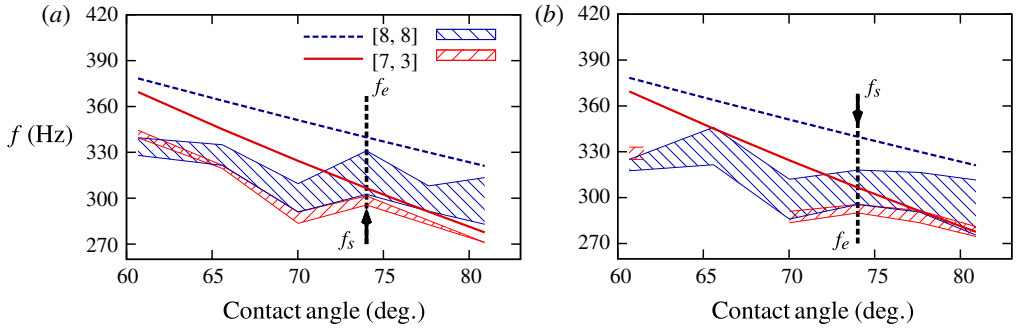

FIGURE 13. (Colour online) Bands (hatched) of modes [8, 8] and [7, 3] for upward (*a*) and downward (*b*) scans, from f_s to f_e. Differences between (*a*) and (*b*) represent hysteresis. Based on (*a*), frequencies cross at $\alpha \approx 60°$–$70°$. In (*b*), there is a gap in the observation of the [7, 3] mode. The [8, 8] mode hysteretically scavenges the [7, 3] mode across the gap, from $\alpha \approx 62°$ to $\alpha \approx 70°$. The lines are inviscid predictions for reference.

the ranges of CAs where these bands cross are separated from other crossings. The protocol in § 3.3 is used. For (i), upward and downward scan results are shown in figure 13(*a*,*b*) respectively. The hatched bands are the observations. As a guide to the eye, we include the inviscid predictions (curves). (The VPF theory predicts bands that cross over the same range of CAs but, for clarity of presentation, we omit these.) In the upward scan, [8, 8] is observed to cross [7, 3] at $\alpha \approx 65°$, figure 13(*a*). In the downward scan at $\alpha \approx 65°$, the [7, 3] mode is missing and the crossing must be inferred from the scans near $\alpha \sim 60°$ and $\alpha > 70°$, where the [7, 3] reappears.

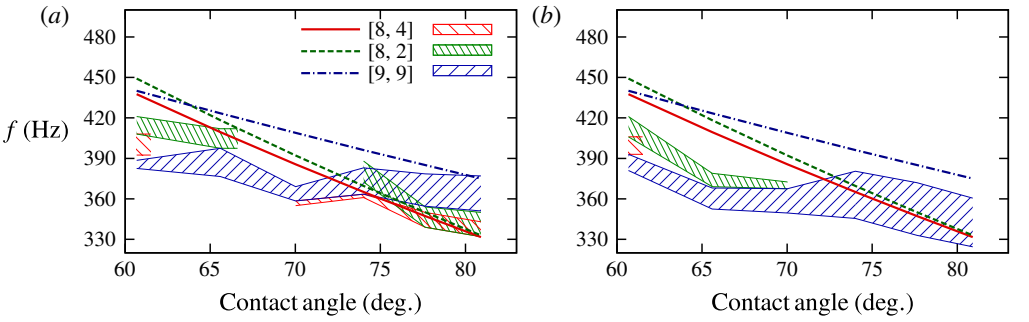

FIGURE 14. (Colour online) Bands (hatched) of modes [9, 9], [8, 2] and [8, 4] by upward (*a*) and downward (*b*) scans. Differences between (*a*) and (*b*) represent hysteresis. Based on (*a*), the frequencies of [9, 9] and [8, 4] cross at $\alpha \approx 60°$–$70°$ and those of [9, 9] and [8, 2] at $\alpha \approx 65°$–$75°$. In (*b*), the gaps in the observed [8, 4] for $\alpha > 60°$ and [8, 2] for $\alpha > 70°$ suggest a hysteretic scavenging of both missing modes by the [9, 9] mode. The lines are inviscid predictions for reference.

Crossing correlates with spectral crowding, which is necessary for mode competition. Competition is observed here where the [7, 3] band disappears from figure 13(*b*). Differences between figures 13(*a*) and 13(*b*) represent hysteresis. In particular, the presence and absence of [7, 3] in figures 13(*a*) and 13(*b*) reveal hysteretic mode competition. One sees that the sectoral [8, 8] mode hysteretically scavenges the [7, 3] mode in the downward scan where their bands cross, $60° \leqslant \alpha \leqslant 70°$. The hysteresis clearly indicates nonlinearity in the resonating sessile drop's pattern selection.

Results of [9, 9] crossing [8, 2] and [8, 4] are shown in figure 14. Similar features are observed. From figure 14(*a*) starting at $\alpha \approx 60°$, [9, 9] is excited at the lowest frequency. As α increases, [9, 9] is observed to hysteretically annex the band of [8, 2] first at approximately $\alpha = 65°$ and then that of [8, 4] at $\alpha = 70°$. According to the upward scans, the crossing between [9, 9] and [8, 4] occurs approximately for $60° \leqslant \alpha \leqslant 70°$. Similarly, [8, 2] crosses [9, 9] for $65° \leqslant \alpha \leqslant 75°$. Further increase of α finally allows the [9, 9] mode to separate from the other two modes completely. The [8, 2] and [8, 4] are observed to mix for $\alpha > 75°$.

The downward scan in figure 14(*b*) reveals mode competition (disappearing bands) similar to that of figure 13(*b*). Only [9, 9] appears for $\alpha > 70°$; the [9, 9] has scavenged the [8, 2] and [8, 4] modes. Another side of this hysteresis is seen in a separate test that varies the forcing acceleration. For $\alpha > 70°$, if one triggers the [9, 9] mode first and then reduces the forcing acceleration sufficiently, the [9, 9] mode disappears. At the same forcing frequency, either [8, 2] or [8, 4] or their mixture replaces [9, 9] when the acceleration is ramped back up to its original level. Hence, we observed a bistability where drops of the same volume subject to the same forcing select a mode according to which one emerges first. This observation is in contrast to the work of Ciliberto & Gollub (1985), where higher frequency modes are reported as the dominant modes when Faraday waves compete.

8. Conclusion

The resonant behaviours of sessile water drops are studied in the regime where motions are primarily inviscid. Drops are mechanically excited using substrate-normal

oscillations produced by a shaker table. Contact lines are pinned using prepared substrates and CAs are controlled by the volume deposited. The observed behaviour is first compared with the predicted eigenfrequencies and eigenmode shapes for the natural oscillations of the inviscid drop of Part 1. Then, to better account for forcing and weak viscous effects, the spectral problem solved in Part 1 is extended using a VPF approximation.

The theory of Part 1 neglects vorticity and the no-slip condition, which naturally brings the relevance of the theory into question. Furthermore, the experiments are conducted in the high-Reynolds-parameter regime where the nonlinearity of the Navier–Stokes equation may play a role. Perhaps surprisingly then, experiment shows a broad relevance of the inviscid linear theory: (i) the first 37 predicted eigenmode shapes are discovered; (ii) the predicted eigenfrequency trends with contact angle are observed; (iii) a linear superposition of eigenmodes to yield mixed modes is documented; (iv) in CA regimes where modal frequencies cross, modes that mix linearly and compete hysteretically are exhibited. On the other hand, the observed resonance frequencies for flatter drops, of higher modes especially, are overpredicted by the inviscid theory. These observations are accommodated by including forcing and weak viscosity through a VPF extension of the theory which yields finite resonant peaks and variable bandwidths.

The experiments demonstrate the relevance of inviscid linear predictions. Modes with isolated resonance bands tend to behave linearly, while those with overlapping bands may behave linearly (mix) or hysteretically (compete). Spectral crowding, as predicted by Part 1 and understood as a symmetry breaking of the Rayleigh–Lamb spectrum, provides a guide to the parameter regimes with the richest modal interactions. As a rule of thumb, modes from different families (e.g. harmonic and subharmonic) tend to mix, while modes from the same family (e.g. subharmonic) tend to compete. In the broad context of the Navier–Stokes equations, the inviscid irrotational theory of Part 1 provides an outer problem that does surprisingly well in describing the droplet responses, even while the existence of rotational motions and boundary layers near the support surface and contact line must be acknowledged. An open question remains: What is the regime of validity for the outer solution? This paper begins to address this question from the experimental viewpoint.

Acknowledgements

A referee is thanked for pointing out the frequency shift literature of the 1980s and 1990s. The authors sincerely acknowledge Dr M. Y. Louge for his generous supply of the VTS-100 mechanical oscillator used in this work. The authors appreciate the constant helpful discussions with and assistance from research specialist G. Swan, Dr B. Land and D. Hartino regarding construction of all custom mechanical and electrical hardware used in this work. The authors acknowledge helpful and inspiring discussions with Dr M. Y. Louge, Dr A. T. Zehnder, Dr W. H. Sachse, Dr K. Boettcher, Dr C. Cohen and colleague D. Lee. Finally, the authors thank NASA (grant no. NNX09AI83G), the National Science Foundation (grant no. CBET-1236582) and the Xerox Corporation for financial support.

Appendix A. Substrate preparation details

The substrates P_{gl} and P_{PC} are implemented to conduct experiments with sub- and superhemispherical drops respectively. Here, the P_{gl} substrates are prepared purely based on manipulation of surface chemistry and incorporate no physical microstructure.

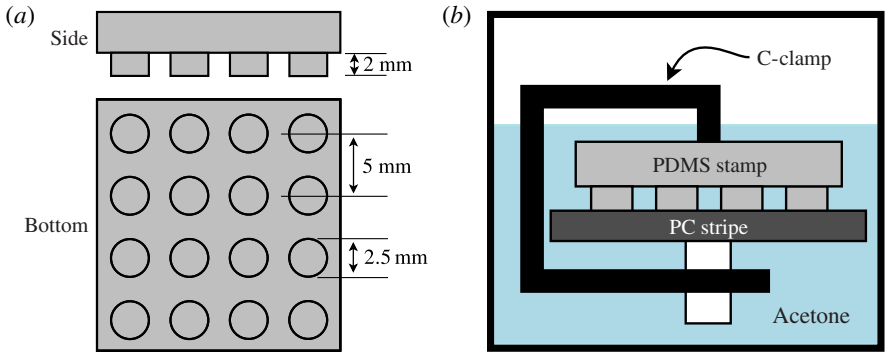

FIGURE 15. (Colour online) Acetone treatment of PC: (*a*) specification of the PDMS stamp used in acetone treatment of PC, (*b*) a PC stripe masked by a PDMS mask and soaked in acetone.

Such substrates are covered by hydrophobic coating except within pinning sites. The implementation starts with sonicating glass slides (VWR VistaVision, catalogue No. 16004-430, $3'' \times 1'' \times 1$ mm, by VWR International LLC, Radnor, PA, USA) for 20 min in deionized (DI) water (purified by ELGA ULTRA SC MK2) to remove residual solid particles. The sonicated slides are subsequently soaked for 20 min in piranha solution (70 % sulphuric acid by volume, BDH3068-500MLP by VWR International LLC, Radnor, PA, USA, and 30 % hydrogen peroxide by volume, 516813-500ML by Sigma-Aldrich, St Louis, MO, USA). Upon completion, the glass slides are rinsed with DI water for at least 10 min and dried by high-purity nitrogen (Airgas, Salem, NH, USA) for subsequent coating. The coating is conducted by first preparing silane mixture consisting of 2 µl of (heptadecafluoro-1,1,2,2-tetrahydrodecyl)trichlorosilane (product code SIH5841.0, by Gelest, Morrisville, PA, USA) in 2 g of light mineral oil (Fisher Scientific, Pittsburgh, PA, USA) and then degassing for 20 min to remove gaseous impurities. The silane is coated onto the cleaned and dried glass slides by chemical vapour deposition (CVD) for at least 5 h. The slides are then heated at 85 °C for 15 min to further secure the coating. To create a pinning site, a coated slide is covered by a soft polymer membrane (made of Sylgard 184 PDMS, by Dow Corning, Midland, MI, USA) with a prescribed circular opening of 5 mm diameter and subsequently treated by oxygen plasma (Harrick Plasma, Ithaca, NY, USA) for 1 min. By the plasma treatment, the coated silane molecules are removed by the plasma within the uncovered circular region, as shown in figure 4. The maximal static contact angle for water drops on a fluoro-silane-coated surface is approximately 105°, which is also the upper limit below which a drop stays pinned on the pinning site.

For experiments with superhemispherical drops, P_{PC} substrates are implemented based on the presence and absence of physical structures. Conceptually, hierarchical physical structures are developed everywhere on P_{PC} except within pinning sites, and hydrophobic coating homogeneously covers the entire surface. The physical structures on P_{PC} are implemented based on solvent-induced recrystallization of PC, as presented in Cui *et al.* (2012). A soft polymer stamp made of Sylgard 184 PDMS (Dow Corning, Midland, MI, USA) with circular pillars is prepared first, as shown in figure 15(*a*). The implementation starts with preparing $3'' \times 1''$ stripes of PC sheets (Makrolon GP-V, by Bayer MaterialScience LLC, Sheffield, MA, USA) and removing

the middle $1'' \times 1''$ of protective film. Very gently, the polymer stamp and the PC stripe are clamped together, with the circular pillars contacting the $1'' \times 1''$ exposed PC surface to shield circular regions in subsequent acetone treatment, as shown in figure 15(*b*). The stripe and the stamp are soaked together in acetone (99.5 % min, by Avantor Performance Materials, Center Valley, PA, USA) for 6 min. Upon completion of acetone treatment, the stamp is removed from the stripe, which is then dried with compressed air thoroughly. Except within the shielded circular regions, patterns of recrystallization should render the acetone-treated PC stripe translucent. The treated PC is then cleaned with ozone plasma (Basic Plasma Cleaner PDC-32G, by Harrick Plasma, Ithaca, NY, USA; oxygen by Airgas, Berwyn, PA, USA) at 600 mTorr (regulated by PlasmaFlo Gas Flow Mixer PDC-FMG, by Harrick Plasma, Ithaca, NY, USA) for 1 min. The same chemical coating is subsequently applied to the plasma-cleaned PC with the same procedure as for P_{gl}, except that at least 40 h must be allowed for CVD. It should be noted that chemical coating is neither applied nor suggested in Cui *et al.* (2012), and sufficiently recrystallized PC surfaces are indeed completely non-wetting for small quasi-statically deposited sessile drops. In the presence of external excitation reaching $30g$ or higher, however, the coating is necessary for preventing sessile drops from spreading on the surface and penetrating into the physical structure of the recrystallized PC. The maximal static contact angle for DI water drops on the silane-coated recrystallized PC surface is approximately 149°. In contrast to the pinning sites on P_{gl}, which are completely transparent, and hence the areas of contrasting surface energies cannot be distinguished without depositing drops, those on P_{PC} are the visually smooth and transparent regions as opposed to its translucent portions elsewhere. Because the pinning sites of P_{PC} are also coated by the fluoro silane, the minimal contact angle of DI water drops is approximately 105°. Therefore, for DI water, the P_{PC} substrates are exclusively used for superhemispherical drops. It should be noticed that for all P_{PC} substrates, the pinning sites are larger than the pillars in the polymer stamps and the sites cannot be precisely controlled. To accommodate the bias, a stamp with pillars of a diameter ($\approx$2.5 mm) smaller than the target size of the footprints (3 mm) is used, and the actual footprint diameter of the pinning site is measured from images after completion of substrate preparation.

The H_{gl} substrates for exploring mode mixing are homogeneously coated with 3-aminopropyltriethoxysilane (APTES, product code SIA0127.0, by Gelest, Morrisville, PA, USA) to achieve a contact angle of DI water drops in the range of 45°–80°. The detailed fabrication procedure can be found in Chang *et al.* (2013).

Appendix B. Comparison of experiment with the inviscid and VPF theories for $k = 9$ modes

Results for modes with $k = 9$ are presented in figure 16. The influence of contact angle on mode emergence remains the same: flatter ($\alpha < 50°$) drops do not exhibit [9, 9] and [9, 7] modes, and only [9, 5], [9, 7] and [9, 9] are observed for $\alpha > 110°$. The absence of [9, 1] and [9, 3] is speculated to result from similar causes as for [7, 1] and [7, 3]. Again, $60° \leqslant \alpha \leqslant 80°$ is where the inviscid theory and experiments best agree, and the predicted bands by the VPF theory capture all observed bands. Here, we emphasize that the observations of the [9, 5], [9, 7] and [9, 9] modes not only serve to test the theories, but also demonstrate the complete reversal of the order of their spectra, as discussed in § 4.

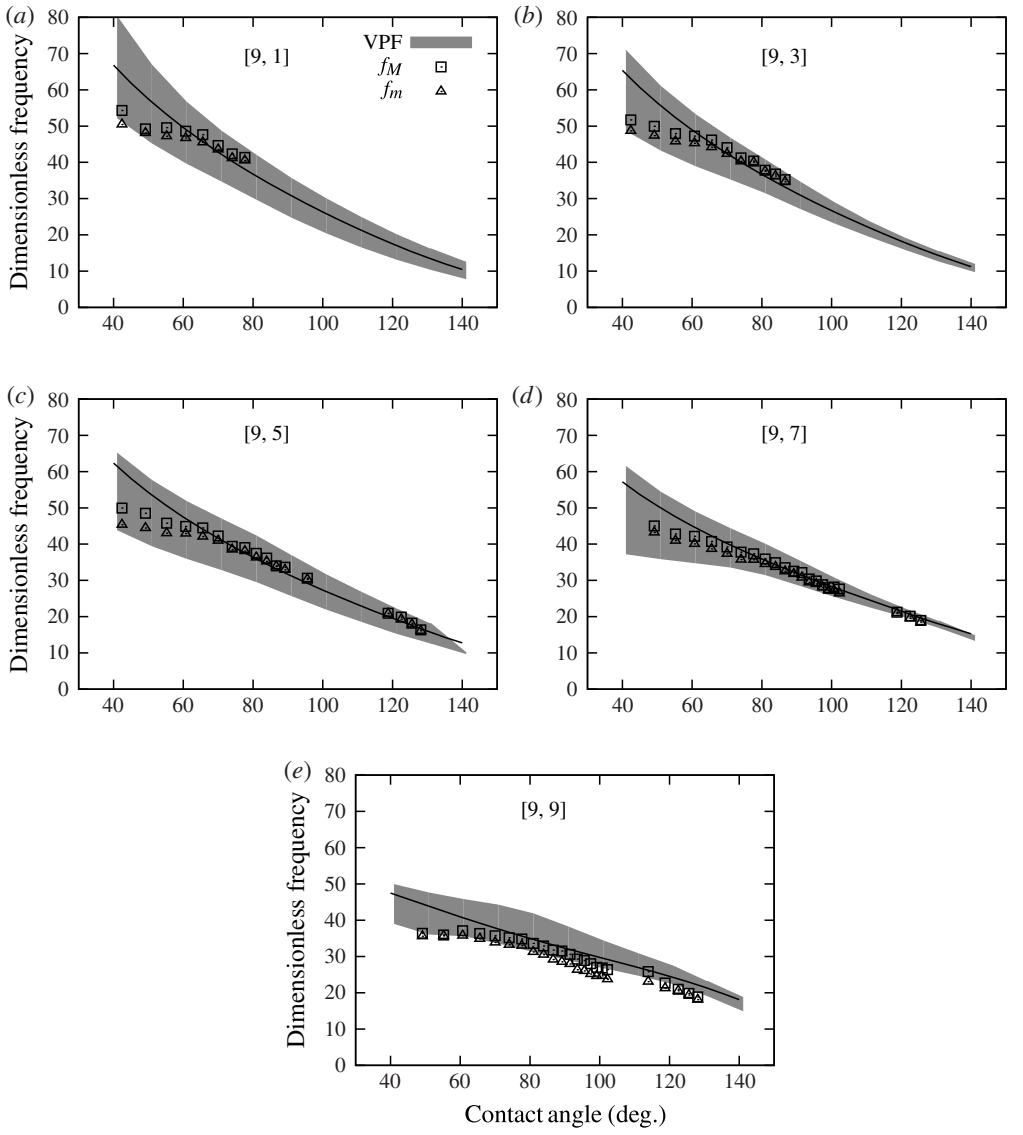

FIGURE 16. Frequency comparisons for $k = 9$ modes, $[9, l]$: VPF theory (shaded bands), inviscid theory (solid lines) and observation (symbols) for (*a*) $l = 1$, (*b*) $l = 3$, (*c*) $l = 5$, (*d*) $l = 7$ and (*e*) $l = 9$. For each mode, f_M and f_m are the observed upper and lower limits of the band.

REFERENCES

ARSCOTT, F. M., SNEDDON, I. N. & ULAM, S. 2014 *Periodic Differential Equations: An Introduction to Mathieu, Lamé, and Allied Functions*. Elsevier Science.

BASARAN, O. A. 2002 Small-scale free surface flows with breakup: drop formation and emerging applications. *AIChE J.* **48** (9), 1842–1848.

BATSON, B., ZOUESHTIAGH, F. & NARAYANAN, R. 2013 The Faraday threshold in small cylinders and the sidewall non-ideality. *J. Fluid Mech.* **729**, 496–523.

BAUER, H. F. 1992 Response of axially excited spherical and conical liquid systems with anchored edges. *Forsch. Ing. Wes.* **58** (4), 96–103.

BENJAMIN, T. B. & URSELL, F. 1954 The stability of the plane free surface of a liquid in vertical periodic motion. *Proc. R. Soc. Lond.* A **225** (1163), 505–515.

BOSTWICK, J. & STEEN, P. 2013 Coupled oscillations of deformable spherical-cap droplets. Part 2. Viscous motions. *J. Fluid Mech.* **714**, 336–360.

BOSTWICK, J. & STEEN, P. 2014 Dynamics of sessile drops. Part 1. Inviscid theory. *J. Fluid Mech.* **760**, 5–38.

BOUWHUIS, W., WINKELS, K., PETERS, I., BRUNET, P., VAN DER MEER, D. & SNOEIJER, J. 2013 Oscillating and star-shaped drops levitated by an airflow. *Phys. Rev.* E **88**, 023017.

BRUNET, P. & SNOEIJER, J. 2011 Star-drops formed by periodic excitation and on an air cushion a short review. *Eur. Phys. J.* B **192** (1), 207–226.

BUSSE, F. H. 1984 Oscillations of a rotating liquid drop. *J. Fluid Mech.* **142**, 1–8.

CASTREJON-PITA, J. R., BAXTER, W. R. S., MORGAN, J., TEMPLE, S., MARTIN, G. D. & HUTCHINGS, I. M. 2013 Future, opportunities and challenges of inkjet technologies. *Atomiz. Sprays* **23** (6), 541–565.

CHANG, C.-T., BOSTWICK, J. B., STEEN, P. H. & DANIEL, S. 2013 Substrate constraint modifies the Rayleigh spectrum of vibrating sessile drops. *Phys. Rev.* E **88**, 023015.

CHEBEL, N. A., RISSO, F. & MASBERNAT, O. 2011 Inertial modes of a periodically forced buoyant drop attached to a capillary. *Phys. Fluids* **23** (10), 102104.

CILIBERTO, S. & GOLLUB, J. P. 1985 Chaotic mode competition in parametrically forced surface waves. *J. Fluid Mech.* **158**, 381–398.

CUI, Y., PAXSON, A. T., SMYTH, K. M. & VARANASI, K. K. 2012 Hierarchical polymeric textures via solvent-induced phase transformation: a single-step production of large-area superhydrophobic surfaces. *Colloids Surf.* A **394** (2012), 8–13.

DANIEL, S., CHAUDHURY, M. K. & CHEN, J. C. 2001 Fast drop movements resulting from the phase change on a gradient surface. *Science* **291** (5504), 633–636.

DANIEL, S., CHAUDHURY, M. K. & DE GENNES, P.-G. 2005 Vibration-actuated drop motion on surfaces for batch microfluidic processes. *Langmuir* **21** (9), 4240–4248; pMID: 15836001.

DONG, L., CHAUDHURY, A. & CHAUDHURY, M. 2006 Lateral vibration of a water drop and its motion on a vibrating surface. *Eur. Phys. J.* E **21** (3), 231–242.

DORBOLO, S., TERWAGNE, D., VANDEWALLE, N. & GILET, T. 2008 Resonant and rolling droplet. *New J. Phys.* **10** (11), 113021.

FENG, J. Q. & BEARD, K. V. 1991 Resonances of a conducting drop in an alternating electric field. *J. Fluid Mech.* **222**, 417–435.

HARTOG, J. P. D. 1956 *Mechanical Vibrations*. McGraw-Hill.

HILL, R. J. A. & EAVES, L. 2010 Vibrations of a diamagnetically levitated water droplet. *Phys. Rev.* E **81**, 056312.

HILL, R. J. A. & EAVES, L. 2012 Shape oscillations of an electrically charged diamagnetically levitated droplet. *Appl. Phys. Lett.* **100** (11), 114106.

HOLTER, N. J. & GLASSCOCK, W. R. 1952 Vibrations of evaporating liquid drops. *J. Acoust. Soc. Am.* **24** (6), 682–686.

JOSEPH, D. 2006 Helmholtz decomposition coupling rotational to irrotational flow of a viscous fluid. *Proc. Natl Acad. Sci. USA* **103**, 14272–14277.

JOSEPH, D. D. 2003 Viscous potential flow. *J. Fluid Mech.* **479**, 191–197.

LAMB, H. 1932 *Hydrodynamics*. Cambridge University Press.

MACROBERT, T. 1967 *Spherical Harmonics*. Pergamon.

MARSTON, P. L. & APFEL, R. E. 1980 Quadrupole resonance of drops driven by modulated acoustic radiation pressure – experimental properties. *J. Acoust. Soc. Am.* **67** (1), 27–37.

NOBLIN, X., KOFMAN, R. & CELESTINI, F. 2009 Ratchetlike motion of a shaken drop. *Phys. Rev. Lett.* **102**, 194504.

PADRINO, J., FUNADA, T. & JOSEPH, D. 2007 Purely irrotational theories for the viscous effects on the oscillations of drops and bubbles. *Intl J. Multiphase Flow* **34**, 61–75.

PEREZ, M., BRECHET, Y., SALVO, L., PAPOULAR, M. & SUERY, M. 1999 Oscillation of liquid drops under gravity: influence of shape on the resonance frequency. *Eur. Phys. Lett.* **47** (2), 189–195.

QI, A., YEO, L., FRIEND, J. & HO, J. 2010 The extraction of liquid, protein molecules and yeast cells from paper through surface acoustic wave atomization. *Lab on a Chip* **10**, 470–476.

RAJCHENBACH, J., CLAMOND, D. & LEROUX, A. 2013 Observation of star-shaped surface gravity waves. *Phys. Rev. Lett.* **110**, 094502.

RAYLEIGH, L. 1879 On the capillary phenomena of jets. *Proc. R. Soc. Lond.* **29** (196–199), 71–97.

RODOT, H., BISCH, C. & LASEK, A. 1979 Zero-gravity simulation of liquids in contact with a solid surface. *Acta Astronaut.* **6**, 1083–1092.

SHARP, J., FARMER, D. & KELLY, J. 2011 Contact angle dependence of the resonant frequency of sessile water droplets. *Langmuir* **27** (15), 9367–9371.

SHEN, C. L., XIE, W. J. & WEI, B. 2010 Parametrically excited sectorial oscillation of liquid drops floating in ultrasound. *Phys. Rev.* E **81**, 046305.

SHI, T. & APFEL, R. E. 1995 Oscillations of a deformed liquid drop in an acoustic field. *Phys. Fluids* **7** (7), 1545–1552.

SHILTON, R., TAN, M. K., YEO, L. Y. & FRIEND, J. R. 2008 Particle concentration and mixing in microdrops driven by focused surface acoustic waves. *J. Appl. Phys.* **104** (1), 014910.

TRINH, E., ZWERN, A. & WANG, T. G. 1982 An experimental study of small-amplitude drop oscillations in immiscible liquid systems. *J. Fluid Mech.* **115**, 453–474.

TRINH, E. H., HOLT, R. G. & THIESSEN, D. B. 1996 The dynamics of ultrasonically levitated drops in an electric field. *Phys. Fluids* **8** (1), 43–61.

VUKASINOVIC, B., SMITH, M. & GLEZER, A. 2007 Dynamics of a sessile drop in forced vibration. *J. Fluid Mech.* **587**, 395–423.

WANG, T. G., ANILKUMAR, A. V. & LEE, C. P. 1996 Oscillations of liquid drops: results from USML-1 experiments in space. *J. Fluid Mech.* **308**, 1–14.

WHITEHILL, J., NEILD, A., NG, T. W. & STOKES, M. 2010 Collection of suspended particles in a drop using low frequency vibration. *Appl. Phys. Lett.* **96** (5), 053501.

WRIGHT, P. H. & SAYLOR, J. R. 2003 Patterning of particulate films using Faraday waves. *Rev. Sci. Instrum.* **74** (9), 4063–4070.

YOSHIYASU, N., MATSUDA, K. & TAKAKI, R. 1996 Self-induced vibration of a water drop placed on an oscillating plate. *J. Phys. Soc. Japan* **65** (7), 2068–2071.